INTERNATIONAL JOURNAL FOR NUMERICAL METHODS IN FLUIDS, VOL. 24, 833–861 (1997)

PEGASE: A NAVIER–STOKES SOLVER FOR DIRECT NUMERICAL SIMULATION OF INCOMPRESSIBLE FLOWS

THIÊN HIÊP LÊ[1], BRUNO TROFF[1], PIERRE SAGAUT[1], KHOA DANG-TRAN[1]* AND LOC TA PHUOC[1]†

[1]*29 Avenue de la Division Leclerc, BP 72, F-92322 Chatillon Cedex, France*

SUMMARY

A hybrid conservative finite difference/finite element scheme is proposed for the solution of the unsteady incompressible Navier–Stokes equations. Using velocity–pressure variables on a non-staggered grid system, the solution is obtained with a projection method based on the resolution of a pressure Poisson equation.

The new proposed scheme is derived from the finite element spatial discretization using the Galerkin method with piecewise bilinear polynomial basis functions defined on quadrilateral elements. It is applied to the pressure gradient term and to the non-linear convection term as in the so-called group finite element method. It ensures strong coupling between spatial directions, inhibiting the development of oscillations during long-term computations, as demonstrated by the validation studies.

Two- and three-dimensional unsteady separated flows with open boundaries have been simulated with the proposed method using Cartesian uniform mesh grids. Several examples of calculations on the backward-facing step configuration are reported and the results obtained are compared with those given by other methods. © 1997 by John Wiley & Sons, Ltd. Int. j. numer. methods fluids 24: 833–861, 1997.

(No. of Figures: 20. No. of Tables: 0. No. of Refs: 23.)

KEY WORDS: Navier–Stokes; incompressible; unsteady; finite difference; finite element; non-staggered grid

1. INTRODUCTION AND BACKGROUND

1.1. Artificial compressibility and pressure Poisson equation

The primitive variable velocity–pressure formulation has been widely adopted for computing the incompressible Navier–Stokes equations and there are two common ways for the numerical resolution of these equations: the artificial compressibility and pressure Poisson equation methods. In both methods the time-dependent momentum equations are calculated using time-marching techniques, while each method employs a different equation to compute the pressure.

Chorin[1] modified the incompressible continuity equation by adding a time derivative term for the pressure. Thus the flow becomes artificially compressible, since pressure waves of finite speed are

* Correspondence to: K. Dang-Tran, ONERA, 29 Avenue de la Division Leclerc, BP 72, F-92332 Chatillon Cedex, France.
† Also at LIMSI-CNRS, BP 133, F-91403 Orsay Cedex, France.

CCC 0271–2091/97/090833–29$17.50 *Received 22 March 1995*

introduced in the incompressible flow field. The resulting system of governing equations is hyperbolic and can be solved by methods developed for compressible flow. This formulation is generally well adapted when only steady solutions are sought.

Harlow and Welch[2] proposed another approach to solve the incompressible Navier–Stokes equations. In this approach the continuity constraint is replaced by a Poisson equation for the pressure. The system of governing equations consists of the parabolic momentum equations and the elliptic pressure Poisson equation, and boundary conditions are required for the pressure.

1.2. Staggered and non-staggered grids

One main difficulty of the primitive variable formulation is the satisfaction of the discrete continuity equation. Harlow and Welch[2] proposed the use of a staggered grid, while Chorin[3] suggested the use of a non-staggered grid associated with a finite difference approach.

Staggered grids have some advantages over non-staggered grids, in particular in the prevention of grid-scale oscillations[2] and the satisfaction of the discrete continuity equation.[4] However, when non-uniform or/and non-orthogonal meshes are used, the task of discretizing the governing equations becomes very complex and possible alternative approaches may be to use semi-staggered or non-staggered grids.[5]

On a non-staggered grid in the artificial compressibility method an explicit fourth-order artificial dissipation term is added to the discrete continuity equation in order to eliminate odd–even decoupling modes in the pressure field due to the central second-order finite difference approximation of the continuity equation. Therefore the discrete divergence of the velocity field is driven to a term proportional to the fourth-order derivative of the pressure.

Similarly, the pressure Poisson method may not satisfy the discrete continuity equation exactly on a non-staggered grid. This can be explained by analysing the method chosen to obtain the discrete pressure equation, either directly from the continuous pressure equation or by taking the discrete divergence of the discrete momentum equation. A careful examination of this problem has been carried out by Sotiropoulos and Abdallah.[6]

Several other works concerning non-staggered grids have been reported in the literature. Strikwerda,[4] Rhies and Chow,[7] Abdallah[8,9] and Armfield[5] have studied the main conditions required for the success of methods based on non-staggered grids, among which integrability and regularity properties appear to be two important constraints which should be satisfied by the discretization procedure.

1.3. Boundary conditions

Another important problem is the choice of proper boundary conditions for the velocity and pressure when using the pressure equation method. An extensive review of this problem may be found in Reference 10.

For a solid boundary the velocity boundary condition is a no-slip condition; for the pressure, standard projection methods lead to a homogeneous Neumann condition, while more sophisticated methods use an inhomogenous Neumann condition. At an outflow boundary and in the absence of body forces, prescribing zero normal and tangential stress components leads respectively to a Dirichlet boundary condition on the pressure and to a Neumann boundary condition on the velocity component tangential to the boundary. These boundary conditions are detailed in Section 2.

Finally, to initiate the computation, an initial field, verifying these boundary conditions has to be computed in order to satisfy the divergence-free condition for the velocity.

1.4. Overview of study

In this paper we present a new hybrid finite difference/finite element scheme for solving the unsteady 3D Navier–Stokes equations in conservative form on a non-staggered grid using the pressure Poisson equation (PPE) formulation.

Section 2 presents the basic equations and associated boundary conditions.

The proposed method, described in Section 3, is based on a conservative finite element scheme for the divergence operator which allows one to eliminate the spurious oscillations induced by a standard finite difference approximation of this operator. The scheme is modified at the near-boundary nodes in order to retain this property.

The time integration is described in Section 4. Some properties of the new scheme are commented upon and basic validation tests are detailed in Section 5.

The efficiency of the present method is demonstrated on the backward-facing step problem (Section 6). Numerical results are compared with those given by other numerical methods and experimental measurements. For Reynolds number $Re = 800$ a steady solution is reached and the results are in good agreement with those reported by Gresho *et al.*[11] and Gartling.[12]

Finally, the feasibility of the method is demonstrated in the 3D case at low Reynolds number by computing the transient flow through a square section ribbed channel (Section 7).

2. GOVERNING EQUATIONS

2.1. Basic equations

The non-dimensionalized Navier–Stokes equations for the unsteady three-dimensional flow of an incompressible fluid in a bounded domain $\bar{\boldsymbol{\Omega}}$ with boundary $\partial\boldsymbol{\Omega} = \boldsymbol{\Gamma} = \boldsymbol{\Gamma}_{\mathbf{D}} + \boldsymbol{\Gamma}_{\mathrm{N}}$ are expressed in Cartesian co-ordinates $\vec{x} = (x, y, z)$ as

$$\vec{\nabla} \cdot \vec{v} = 0 \quad \text{in } \Omega, \tag{1}$$

$$\frac{\partial \vec{v}}{\partial t} + \vec{\nabla} \cdot (\vec{v} \otimes \vec{v}) = -\vec{\nabla} p + \frac{1}{Re} \nabla^2 \vec{v} \quad \text{in } \Omega, \tag{2}$$

where $\vec{v} = (u, v, w)^{\mathrm{T}}$ is the velocity vector, p is the kinematic pressure (divided by the density) and $\vec{v} \otimes \vec{v}$ is the tensor product of velocity vectors. These equations are subject to the boundary conditions (without external body force)

$$\vec{v} = \vec{W} \quad \text{on } \Gamma_{\mathrm{D}}, \tag{3}$$

$$-p + \frac{1}{Re} \frac{\partial v_n}{\partial \vec{n}} = 0 \quad \text{on } \Gamma_{\mathrm{N}}, \tag{4}$$

$$\frac{1}{Re} \frac{\partial v_\tau}{\partial \vec{n}} = 0 \quad \text{on } \Gamma_{\mathrm{N}}, \tag{5}$$

where $\vec{W}$ is a prescribed velocity, and to the initial conditions

$$\vec{v}(\vec{x}, 0) = \vec{v}_0(\vec{x}) \quad \text{in } \bar{\Omega}, \tag{6}$$

$$\vec{\nabla} \cdot \vec{v}_0 = 0 \quad \text{in } \Omega, \tag{7}$$

where $\vec{n}$ is the outward normal unit vector, $v_n = \vec{v} \cdot \vec{n}$ and $v_\tau = \sqrt{(\vec{v} \cdot \vec{v} - v_n^2)}$. The Reynolds number $Re = \bar{V}L/\nu$ is based on the characteristic velocity $\bar{V}$ and length L.

The first condition (4) on boundary Γ_N has been obtained by prescribing a zero normal stress component. The second condition (5) is an approximation of the zero-tangential-stress condition

$$\sigma_\tau = \frac{1}{Re}\left(\frac{\partial v_\tau}{\partial \vec{n}} + \frac{\partial v_n}{\partial \vec{\tau}}\right) = 0, \tag{8}$$

where $\vec{\tau}$ is the tangential unit vector. As the conventional form for the viscous term is employed instead of the stress divergence form, this boundary condition is used for simplicity and is valid in the absence of body force.

2.2. Pressure equation

The pressure equation is derived by applying the divergence operator to the momentum equations, giving a Poisson-type second-order elliptic equation

$$-\nabla^2 p = \vec{\nabla}\cdot\left(\vec{\nabla}\cdot(\vec{v}\otimes\vec{v}) + \frac{\partial}{\partial t}\vec{v} - \frac{1}{Re}\nabla^2\vec{v}\right). \tag{9}$$

By taking advantage of the fact that the divergence and Laplacian operators commute in the continuum, the divergence of the viscous term can be omitted in equation (9). This procedure is common to most existing methods based on the PPE formulation.[13,14] In contrast, the consistent pressure Poisson equation (CPPE) formulation (9)[10] retains this term, which implies additional discretization effort. In Section 5.3 we show that in the case of the proposed scheme this additional effort is not necessary and the divergence of the viscous term may be omitted.

The pressure boundary conditions are of Neumann type on Γ_D and of Dirichlet type on Γ_N. Applying the normal component of momentum on the boundary Γ_D and the zero-normal-stress condition (4) on Γ_N, we obtain

$$\frac{\partial p}{\partial \vec{n}} = \vec{n}\cdot\left(\frac{1}{Re}\nabla^2\vec{v} - \vec{\nabla}\cdot(\vec{v}\otimes\vec{v}) - \frac{\partial \vec{v}}{\partial t}\right) \quad \text{on } \Gamma_D, \tag{10}$$

$$p = \frac{1}{Re}\frac{\partial v_n}{\partial \vec{n}} \quad \text{on } \Gamma_N. \tag{11}$$

2.3. Initialization procedure

For an 'impulsive start' problem such as the transient backward-facing step the initial velocity field is not divergence-free. Following Gresho,[13] a divergence-free initial velocity field $\vec{v}_0$ may be obtained by the following procedure. Let $\vec{u}_0$ be an arbitrary velocity field which may be expressed as the sum of a divergence-free field $\vec{v}_0$ and a solenoidal field $-\vec{\nabla}\lambda$:

$$\vec{u}_0 = \vec{v}_0 - \vec{\nabla}\lambda. \tag{12}$$

The field $\vec{v}_0$ verifies the incompressibility condition if λ is a solution of the equation

$$-\nabla^2\lambda = \vec{\nabla}\cdot\vec{u}_0, \tag{13}$$

subject to the boundary conditions (BCs)

$$\frac{\partial \lambda}{\partial \vec{n}} = 0 \quad \text{on } \Gamma_D, \tag{14}$$

$$\lambda = 0 \quad \text{on } \Gamma_N. \tag{15}$$

However, in practice, this procedure does not always allow one to properly initiate the computation, because the arbitrary initial field $\vec{u}_0$ may not be regular enough. In order to avoid this difficulty, we propose here a predictor step to generate a smooth field $\vec{u}_0$ by solving the Laplacian problem

$$\nabla^2 \vec{u}_0 = 0, \tag{16}$$

with the same BCs (3) and (5) as for the primitive problem.

3. SPATIAL DISCRETIZATION

The assumed rectangular computational domain is discretized on a non-staggered uniform Cartesian grid. Indices i, j, k ($1 \leqslant i \leqslant I_{\max}, 1 \leqslant j \leqslant J_{\max}, 1 \leqslant k \leqslant K_{\max}$) are related to directions x, y, z respectively and $u_{i,j,k}$ is the value of the variable u at the nodal point (i, j, k). An example is given in Figure 4 of Dirichlet (Γ_D) and Neumann (Γ_N) boundaries (as defined in Section 2.1) for the computation of the flow over a backward-facing step.

3.1. First-order derivatives

3.1.1. Oscillations induced by centred finite difference schemes. All first-order derivatives appearing as contributions of the divergence operator of the convective term, of the pressure gradient operator in the momentum equations or of the velocity divergence term in the Poisson equation must be carefully approximated. The standard approximation is written here in the 2D case for dummy variables ϕ and ψ as

$$\left(\frac{\partial \phi}{\partial x}\right)_{i,k} + \left(\frac{\partial \psi}{\partial z}\right)_{i,k} = \delta_x \phi_{i,k} + \delta_z \psi_{i,k} + O(\Delta x^2) + O(\Delta z^2), \tag{17}$$

where δ_x (δ_z) is the standard central difference operator in direction x (z) and

$$\delta_x \phi_{i,k} + \delta_z \psi_{i,k} = \frac{1}{2\Delta x}(\phi_{i+1,k} - \phi_{i-1,k}) + \frac{1}{2\Delta x}(\psi_{i,k+1} - \psi_{i,k-1}). \tag{18}$$

Using this scheme (Figure 1(a)) may lead to oscillations due to the separation of $(i + k)$-odd and $(i + k)$-even nodes (Figure 1(b)).

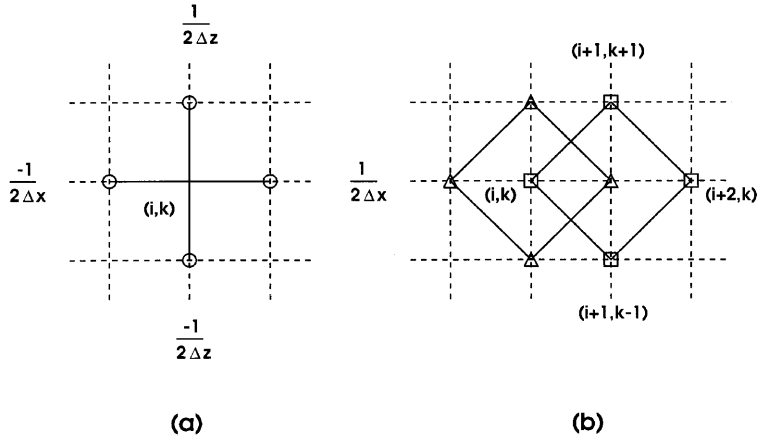

Figure 1. First-derivative standard scheme. (a) Divergence operator molecule. (b) Separation of odd–even nodes: Δ, $i + k$ odd; $\square$, $i + k$ even

3.1.2. Proposed hybrid FEM/FDM centred scheme. Many other schemes derived from finite volume or finite element approaches have been proposed which overcome this difficulty.[15]

In the present study we use an intrinsically multidimensional second-order centred scheme denoted by $\delta^*_{(\cdot)}$ and defined in the 2D case as

$$\delta_x^*\phi_{i,k} + \delta_z^*\psi_{i,k} = \frac{1}{12\Delta x}[(\phi_{i+1,k+1} - \phi_{i-1,k+1}) + 4(\phi_{i+1,k} - \phi_{i-1,k}) + (\phi_{i+1,k-1} - \phi_{i-1,k-1})] + \frac{1}{12\Delta z}[(\psi_{i+1,k+1} - \psi_{i+1,k-1}) + 4(\psi_{i,k+1} - \psi_{i,k-1}) + (\psi_{i-1,k+1} - \psi_{i-1,k-1})]. \quad (19)$$

This scheme is derived from the finite element spatial discretization using the Galerkin method via the expansion of a dummy variable in the piecewise bilinear polynomial basis functions defined on quadrilateral elements. The nodes of the elements are the same as the basic nodes of the finite difference grid and the quadrature rule used is an exact integration formula.

The final stencil obtained for the discrete divergence operator is more complicated than the standard one: it corresponds to an eight-point molecule in 2D, as shown in Figure 2, and a 26-point molecule in 3D, while the standard scheme has a four-point molecule in 2D. It ensures strong coupling between spatial directions, inhibiting the development of oscillations during long-term computations, as demonstrated by the validation studies in Section 6.

In the 3D case the scheme is defined as

$$\begin{aligned}\delta_x^*\phi_{i,j,k} = \frac{1}{72\Delta x}[&(\phi_{i+1,j+1,k+1} - \phi_{i-1,j+1,k+1}) + 4(\phi_{i+1,j,k+1} - \phi_{i-1,j,k+1}) \\ &+ (\phi_{i+1,j-1,k+1} - \phi_{i-1,j-1,k+1}) + 4(\phi_{i+1,j+1,k} - \phi_{i-1,j+1,k}) + 16(\phi_{i+1,j,k} - \phi_{i-1,j,k}) \\ &+ 4(\phi_{i+1,j-1,k} - \phi_{i-1,j-1,k}) + (\phi_{i+1,j+1,k-1} - \phi_{i-1,j+1,k-1}) + 4(\phi_{i+1,j,k-1} - \phi_{i-1,j,k-1}) \\ &+ (\phi_{i+1,j-1,k-1} - \phi_{i-1,j-1,k-1})]. \end{aligned} \quad (20)$$

It corresponds to a 26-point molecule, while the standard scheme has a six-point molecule.

Although a standard FEM methodology has been adopted to compute the proposed scheme, the present approach has two main differences compared with the conventional FEM. The first difference is in the treatment of the discrete boundary conditions: they are not derived from the FEM, but from FDM schemes. The second difference is the treatment of the non-linear convective terms u^2 and uv: the scheme is applied also to these terms as in the so-called group finite element method (GFEM),[16] leading to simpler and less expensive computations. Owing to the basically FDM approximation used, the mass matrix is a diagonal matrix and a lumping method is not employed.

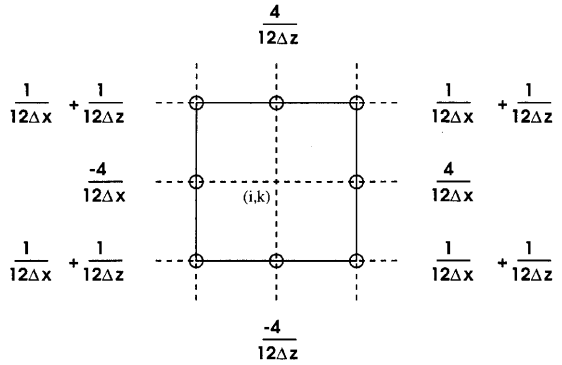

Figure 2. First-derivative hybrid FEM/FDM scheme. Divergence operator molecule

3.2. Second-order and mixed derivatives

The second-order derivatives of the Laplacian operator and the mixed derivatives occurring in the momentum equations and pressure equation are discretized by centred, second-order-accurate schemes which can be obtained by both FDM and FEM (using bilinear basis functions and trapezoidal rule integration) approaches.

3.2.1. Second-order derivatives. In the 2D case we have

$$\left(\frac{\partial^2\phi}{\partial x^2}\right)_{i,k} = \delta_{xx}\phi_{i,k} + O(\Delta x^2), \tag{21}$$

with

$$\delta_{xx}\phi_{i,k} = \frac{1}{\Delta x^2}(\phi_{i+1,k} - 2\phi_{i,k} + \phi_{i-1,k}). \tag{22}$$

For the Laplacian operator the scheme is the standard five-point molecule (in contrast with the nine-point one obtained with an exact integration when the FEM is used):

$$\left(\frac{\partial^2\phi}{\partial x^2}\right)_{i,k} + \left(\frac{\partial^2\phi}{\partial x^2}\right)_{i,k} = \delta_{xx}\phi_{i,k} + \delta_{zz}\phi_{i,k} + O(\Delta x^2) + O(\Delta x^2). \tag{23}$$

3.2.2. Mixed derivatives. Similarly, for the mixed derivatives the scheme is obtained from a combination of elementary schemes applied in both directions x and z. It leads to the simplest centred four-point formula involving the corners of the quadrilateral whose centroid is located at the current point:

$$\left(\frac{\partial^2\phi}{\partial x\partial z}\right)_{i,k} = \delta_{xz}\phi_{i,k} + O(\Delta x\Delta z), \tag{24}$$

with

$$\delta_{xz}\phi_{i,k} = \frac{1}{4\Delta x\Delta z}(\phi_{i+1,k+1} - \phi_{i-1,k+1} - \phi_{i+1,k-1} + \phi_{i-1,k-1}). \tag{25}$$

Extensions of the previous schemes to the 3D case are straightforward.

3.3. Discrete boundary conditions

For any specific problem it is necessary to supply an appropriate set of initial and boundary conditions. We shall be concerned particularly with a prescribed set of no-slip walls and with inflow and outflow boundaries. The rigid walls may partially confine the fluid or they may define an obstacle about which the fluid flows. Inflow boundaries have prescribed conditions of fluid influx through them, while outflow boundaries are arranged in such a way that the fluid outflux through them will occur with minimal disturbance to the fluid remaining in the computational domain.

3.3.1. Velocity boundary conditions. The rigid wall boundary conditions are simple to derive. They follow directly from the momentum equations. For a no-slip wall the tangential and normal velocity components must vanish. Discrete corresponding boundary conditions on the pressure are described hereafter.

Conditions along an inflow boundary are similarly derived. The only difference is that the velocity components are prescribed in some arbitrary manner. Discrete pressure boundary conditions are derived in such a way as to again insure consistency with the momentum balance.

An outflow boundary condition, in contrast, is very difficult to derive, because there is no unique criterion which may help to its formulation. Following equation (5), the normal derivative of the tangential velocity component is enforced to vanish. The normal velocity component is extrapolated from the inner computational domain. These conditions are discretized as described below.

In order to approximate the normal derivatives appearing in (5) for the outflow condition on the right-hand side of the computational domain (which is a vertical line or plane ($i = I_{\max}$)), the tangential component $w_{I_{\max},k}$ is evaluated using an upwind second-order discretization, leading to

$$w_{I_{\max},k} = \tfrac{1}{3}(4w_{i_{\max}-1,k} - w_{I_{\max}-2,k}), \tag{26}$$

and the normal component $u_{I_{\max},k}$ is calculated via the extrapolation formula

$$u_{I_{\max},k} = 3u_{I_{\max}-1,k} - 3u_{I_{\max}-2,k} + u_{I_{\max}-3,k}. \tag{27}$$

This formula corresponds to prescribing the third-order derivative of the normal velocity component equal to zero at the boundary and implicitly involves zero velocity divergence at this boundary.

This procedure completely achieves the computation of the velocity field.

3.3.2. Pressure boundary conditions. As mentioned by Gresho and Sani,[10] the proper choice of pressure boundary conditions and their discrete equivalent counterpart is crucial in the success of a numerical method. We use the continuous boundary conditions proposed by these authors: at an inflow boundary Γ_D or at a rigid wall a Dirichlet boundary condition on velocity leads to a Neumann condition on pressure, while at an outflow boundary Γ_N a Neumann condition on velocity leads to a Dirichlet condition on pressure.

At an outflow boundary the derivation of the discrete boundary condition is straightforward, with a Dirichlet condition (11) on pressure.

The Neumann pressure boundary condition is directly incorporated into the FDM scheme at internal points adjacent to the boundaries. In the 2D case at nodes $(2, k)$ the pressure equation is discretized as

$$-\left[\frac{\partial}{\partial x}\left(\frac{\partial p}{\partial x}\right)\right]_{2,k} - \left(\frac{\partial^2 p}{\partial z^2}\right)_{2,k} = (\mathrm{RHS})_{2,k}, \tag{28}$$

where RHS stands for the right-hand side of the Poisson equation (9).

The second term on the left-hand side is typically a second-order derivative and is discretized with a standard scheme according to (21).

The first term on the left-hand side is a normal derivative which is approximated by a second-order-accurate half-integer central difference scheme:

$$\frac{\partial}{\partial x}\left(\frac{\partial p}{\partial x}\right)_{2,k} = \frac{1}{\Delta x}\left[\left(\frac{\partial p}{\partial x}\right)_{5/2,k} - \left(\frac{\partial p}{\partial x}\right)_{3/2,k}\right] + O(\Delta x^2). \tag{29}$$

The normal derivative in equation (28) at $i = \frac{5}{2}$ is approximated by the central difference scheme (18):

$$\left(\frac{\partial p}{\partial x}\right)_{5/2,k} = \delta_x p_{5/2,k} + O(\Delta x^2), \tag{30}$$

with

$$\delta_x p_{5/2,k} = \frac{1}{\Delta x}(p_{3,k} - p_{2,k}) = \delta_x^+ p_{2,k}. \tag{31}$$

The normal derivative at $i = \frac{3}{2}$ is approximated by a first-order extrapolation procedure:

$$\left(\frac{\partial p}{\partial x}\right)_{3/2,k} = \left(\frac{\partial p}{\partial x}\right)_{1,k} + O(\Delta x) = (\mathrm{BC})_{1,k} + O(\Delta x), \tag{32}$$

where the term $(\partial p/\partial x)_{1,k}$ is evaluated by the pressure boundary condition (10) denoted by $(\mathrm{BC})_{1,k}$.

Equation (27) is thus discretized by

$$-\left(\frac{\delta_x^+}{\Delta x} + \delta_{zz}\right)p_{2,k} = (\mathrm{RHS})_{2,k} - \frac{1}{\Delta x}(\mathrm{BC})_{1,k}. \tag{33}$$

The global second-order spatial accuracy of the method even when using the first-order extrapolation method is demonstrated by Gustafsson.[17]

4. TIME INTEGRATION

The velocity field is computed with the explicit first-order forward Euler scheme. Here a first-order time-accurate method is employed to decouple the velocity and pressure and to enforce the incompressibility constraint of the flow. Such a time scheme is a suitable candidate to run on modern massively parallel machines, giving them a new interest. It should be noted that the obtention of an actual second-order-accurate global temporal scheme and the derivation of the associated boundary conditions are still open problems.[18,19]

4.1. Velocity

The velocity at time $t = (n+1)\Delta t$ is obtained via

$$\vec{v}^{n+1} = \vec{v}^n - \Delta t\left(D^* p^n + D^*(\vec{v} \otimes \vec{v})^n - \frac{1}{Re} L\vec{v}^n\right), \tag{34}$$

where D^* and L are discrete operators defined by

$$D^* = (\delta_x^*, \delta_z^*)^{\mathrm{T}}, \tag{35}$$

$$L = \delta_{xx} + \delta_{zz}. \tag{36}$$

It may be noticed that as soon as the pressure is known at each node, then equation (34) is immediately appropriate for the calculation of new velocities, a process accomplished by simple algebraic substitutions.

4.2. Pressure

The discrete equation is derived from equation (9), in which the term $\partial(\vec{\nabla}\cdot\vec{v})/\partial t$ is discretized by $(D^*\cdot\vec{v}^{n+1}-D^*\cdot\vec{v}^n)/\Delta t$. Setting $D^*\cdot\vec{v}^{n+1}=0$, in order to satisfy the discrete continuity equation, one obtains

$$-(\delta_{xx}+\delta_{zz})p^n_{i,k}=\delta_{xx}(u^2)^n_{i,k}+\delta_{zz}(w^2_{i,k})^n+2\delta_{xz}(uw)^n_{i,k}-\frac{1}{\Delta t}(\delta^*_x u^n_{i,k}+\delta^*_z w^n_{i,k})$$
$$-\frac{1}{Re}[\delta_x(\delta_{xx}+\delta_{zz})u^n_{i,k}+\delta_z(\delta_{xx}+\delta_{zz})w^n_{i,k}]. \tag{37}$$

Since the continuity equation is not directly satisfied, $D^*\cdot\vec{v}^n$ is retained here as a corrective term to prevent the accumulation of numerical errors which lead to instabilities in the solution of the momentum equations.[2,8,9]

A conjugate gradient Bi-CGSTAB algorithm[20] is used to solve the linear system associated with (37).

5. MAIN PROPERTIES OF SCHEME

For simplicity we suppose that $\Delta x=\Delta z$.

5.1. Accuracy and smoothing properties

The leading terms of the truncation error of the first-derivative operator for a scalar dummy variable ϕ defined by (19) are calculated by a Taylor series expansion. For the uniform grid case we obtain for the x-derivative operator

$$(\delta^*_x\phi)_{ik}=\left(\frac{\partial\phi}{\partial x}\right)_{ik}+\frac{\Delta x^2}{6}\left(\frac{\partial^3\phi}{\partial x^3}\right)_{ik}+\frac{\Delta x^2}{6}\left(\frac{\partial^3\phi}{\partial x\partial z^2}\right)_{ik}+O(\Delta x^4). \tag{38}$$

A similar expansion in the z-direction leads to

$$(\delta^*_z\phi)_{ik}=\left(\frac{\partial\phi}{\partial z}\right)_{ik}+\frac{\Delta x^2}{6}\left(\frac{\partial^3\phi}{\partial z^3}\right)_{ik}+\frac{\Delta x^2}{6}\left(\frac{\partial^3\phi}{\partial z\partial x^2}\right)_{ik}+O\,(\Delta x^4). \tag{39}$$

It should be noticed that the truncation error of the discrete divergence operator has the particular form

$$(D^*\cdot\vec{v})_{ik}=(\vec{\nabla}\cdot\vec{v})_{ik}+\frac{\Delta x^2}{6}\nabla^2(\vec{\nabla}\cdot\vec{v})_{ik}+O(\Delta x^4). \tag{40}$$

This result shows that for a locally divergence-free velocity field the term $\nabla^2(\vec{\nabla}\cdot\vec{v})_{ik}$ is vanishing and then the scheme is locally fourth-order-accurate.

Moreover, the discrete divergence operator (44) can be rewritten as

$$(D^*\cdot\vec{v})_{ik}=\left(1+\frac{\Delta x^2}{6}\nabla^2\right)(\vec{\nabla}\cdot\vec{v})_{ik}. \tag{41}$$

By inspection it can be seen that a non-divergence-free velocity will be smoothed by the operator $1+(\Delta x^2/6)\nabla^2$.

5.2. *Stability considerations*

A pragmatic stability criterion may be obtained for the present method in the framework of linear Fourier analysis.

Applying (34) to the scalar advection–diffusion equation

$$\frac{\partial \phi}{\partial t} + \vec{v} \cdot \vec{\nabla} \phi = \frac{1}{Re} \nabla^2 \phi, \tag{42}$$

where $\vec{v} = (u, w)^{\mathrm{T}}$, we obtain

$$\phi^{n+1} = \phi^n - \Delta t \left(uD^* + wD^* - \frac{1}{Re} L \right) \phi^n, \tag{43}$$

where D^* and L defined by (19) and (23) are applied, using a uniform mesh spacing Δx.

As shown in the Appendix, the amplification factor $G(i, k)$ of the present scheme for the mode (i, k) $(0 \leqslant i, k \leqslant N)$ is a function of the u-based cell Reynolds number $Re_u = u\Delta x/v$ and CFL number $\sigma_u = u\Delta t/\Delta x$. Figure 3 displays the stability diagram obtained, given by the $|G(i, k)| \leqslant 1$ condition, in the σ_u versus Re_u plane for different values of the parameter $\sigma_w/\sigma_u = w/u$.

Following this analysis, the scheme is submitted to rather restrictive stability constraints. For small values of σ_u and Re_u, stability is achieved. Maximal CFL numbers of order 0·5 are related to a cell Reynolds number of order 2. Higher cell Reynolds numbers of order 10 may be used if the CFL number is reduced to 0·1.

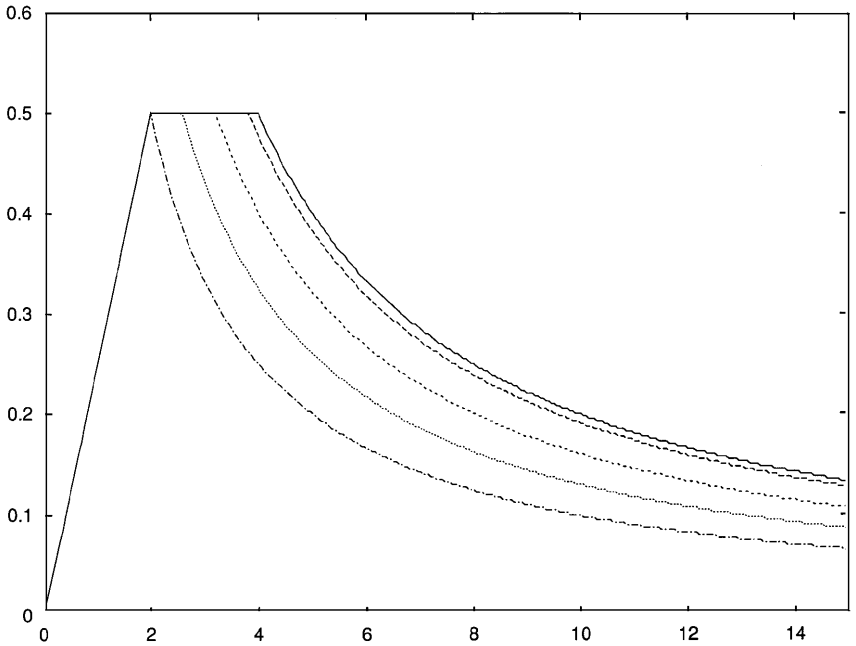

Figure 3. Stability diagram for hybrid scheme. CFL number $\sigma_u = u\Delta t/\Delta x$ versus cell Reynolds number $Re_u = u\Delta x/v$. Theoretical results: ————, $w/u = 0$; – – –, $w/u = 0{\cdot}25$; - - - -, $w/u = 0{\cdot}5$; . . . . , $w/u = 0{\cdot}75$; -·-·-, $w/u = 1$

5.3. Estimation of viscous term in proposed CPPE formulation

The problem of the choice of the PPE or CPPE formulation has been mentioned in Section 2.2. While the continuous problem of the form of the transient heat equation for $\vec{\nabla}\cdot\vec{v}$ has already been studied,[10] the corresponding discrete problem has been poorly argued. It will be proved here in the 2D case that the use of the CPPE approach associated with our spatial scheme leads to the PPE approach for the internal nodes.

In fact, using the discretized equation (37) and adding the viscous term discretized by a second-order scheme, the CPPE equivalent differential equation should read (with $\Delta x = \Delta z$)

$$-\nabla^2 p = \vec{\nabla}\cdot\vec{\nabla}\cdot(\vec{v}\otimes\vec{v}) - \frac{\vec{\nabla}\cdot\vec{v}}{\Delta t} - \left(\frac{1}{6}\frac{\Delta x^2}{\Delta t} + \frac{1}{Re}\right)\vec{\nabla}\cdot\nabla^2\vec{v} + O\left(\Delta x^2, \frac{\Delta x^4}{\Delta t}\right). \tag{44}$$

Equation (44) exhibits competitions between the first term of the truncation error of $D^*\cdot\vec{v}^n/\Delta t$ as given by (40) and the viscous term appearing in the CPPE formulation. The interest of keeping the viscous term in the pressure equation will depend on the balance between the two factors $\Delta x^2/6\Delta t$ and $1/Re$.

The time step Δt may be evaluated by using the two-dimensional stability criterion for the forward Euler scheme given by Hindmarsh *et al.*[21] (see Appendix):

$$\Delta t \leqslant \min(\alpha;\beta), \tag{45}$$

with

$$\alpha = \frac{2\nu}{(u^2+w^2)}, \qquad \beta = Re\frac{\Delta x^2}{4} = \frac{\Delta x^2}{4\nu}. \tag{46}$$

Two cases may be considered: $\beta \leqslant \alpha$ and $\alpha \leqslant \beta$. In the case $\beta \leqslant \alpha$ the cell Reynolds numbers Re^* of the flow is found to be

$$Re^* = \frac{\Delta x\sqrt{[\mathrm{Max}(u^2+w^2)]}}{\nu} \geqslant \sqrt{8}.$$

From (44) we may deduce that the numerical error is at least two-thirds of the viscous CPPE term:

$$\frac{1}{6}\frac{\Delta x^2}{\Delta t} \geqslant \frac{2}{3}\frac{1}{Re}. \tag{47}$$

In the case $\alpha \leqslant \beta$ the cell Reynolds number is $Re^* \leqslant \sqrt{8}$ and (47) still holds.

In both cases the numerical error is far from being negligible with respect to the viscous CPPE term, so that the supplementary work involved in the CPPE approach may not be fully justified except perhaps for very-low-Reynolds-number flows.

6. VALIDATION OF METHOD

6.1. Backward-facing step (BFS) flow configuration

In order to validate the method, the flow over a two-dimensional backward-facing step has been studied. This configuration, for which several experimental and numerical results are available, involves recirculating flow regions and vortex-shedding phenomena. These two generic features, encountered in most flows of practical engineering interest, make the backward-facing step both a relevant and severe test case for numerical methods.

Figure 4 displays the flow geometry and boundary conditions, which correspond to those defined in the Second Minisymposium on Open Boundary Conditions.[22] The expansion ratio $H/h = 2$ and the

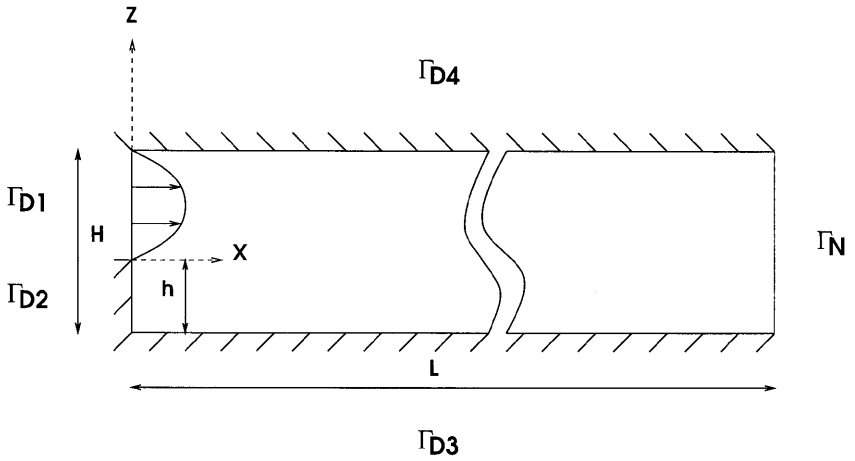

Figure 4. Flow geometry and velocity boundary conditions. 'Dirichlet boundary $\Gamma_{D_1} : u(z) = 24z(0{\cdot}5H - z), w = 0$. 'Dirichlet' boundary $\Gamma_{D_2} : u = w = 0$. 'Dirichlet' boundary $\Gamma_{D_3} : u = w = 0$. 'Dirichlet' boundary $\Gamma_{D^4:u=w=0}$. 'Neumann' boundary $\Gamma_N : -p + \nu\partial u/\partial x = 0, \partial w/\partial x = 0$

channel length/height ratio $L/H = 20$. A parabolic inlet velocity profile, no-slip conditions on solid walls and the outflow boundary conditions (25), (26) and (32) are used. The Reynolds number is based on the mean inlet velocity and H. The computations are performed on an (801×41)-point regular mesh grid with a time step $\Delta t = 5 \times 10^{-4} (\sigma_u = 0{\cdot}02)$ up to 400 time units.

The procedure described in Section 2.3 is used to initialize the computation. The initial vorticity field displays vortex sheets near the channel boundaries as shown in Figure 5.

6.2. Preliminary tests

Before performing the computations, several preliminary tests were done in order to illustrate some properties of the scheme. The cell Reynolds number criterion is illustrated in Figure 6, where the pressure distributions are displayed at $t = 10$. At this time the computation performed with $\sigma_u = 0{\cdot}02$ and $Re_u = 10$ is stable. Increasing the Reynolds number to $Re_u = 30$ leads to a spurious result at $t = 10$.

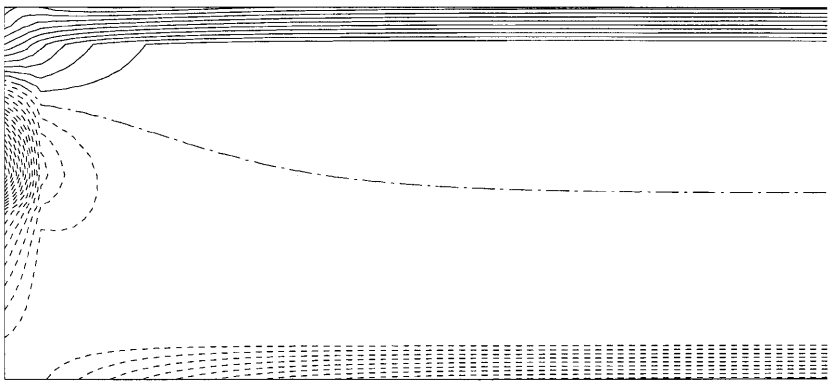

Figure 5. Initial vorticity field (iso-contours)

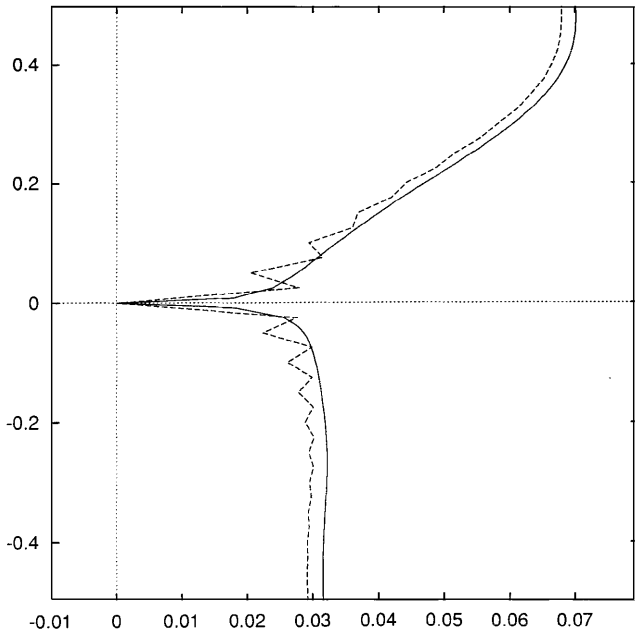

Figure 6. Preliminary tests: cell Reynolds number criterion. Pressure distribution at inlet plane at $t = 10$ (Z-co-ordinate versus P): ————, $\sigma_u = 0{\cdot}02$, $Re_u = 10$; - - - -, $\sigma_u = 0{\cdot}02$, $Re_u = 30$

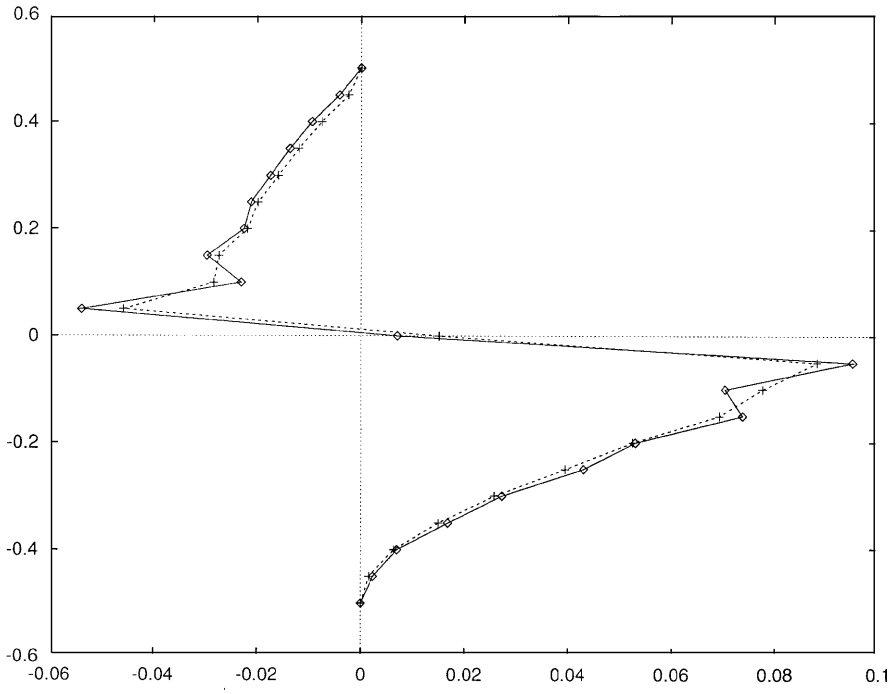

Figure 7. Influence of spatial discretization method. Vertical velocity component distribution at inlet plane (Z-co-ordinate versus w): ◇, standard scheme, $Re_u = 10$; ×, hybrid scheme, $Re_u = 10$

Figure 7 displays the vertical velocity component distributions at the inlet plane obtained at $Re_u = 10$ with a standard FDM discretization and with the present hybrid scheme. Using the present scheme greatly reduces the spatial oscillations induced by the boundary condition discontinuity at the inlet plane.

6.3. *Results and comparisons*

Computations have been performed for the laminar regime $100 \leqslant Re \leqslant 800$. Results obtained for the steady as well as the transient regimes are compared with available experimental and numerical results.

6.3.1. Reattachment length in laminar regime. The Reynolds number dependence of the reattachment length X_r/H is reported in Figure 8. Good agreement is found with the experimental results of Armaly *et al.*[23] for Reynolds numbers up to 400. For higher Reynolds numbers the flow observed in the experiments is three-dimensional, which may explain the discrepancies observed with the 2D calculation.

6.3.2. Transient flow. At $Re = 800$ the transient flow behind the BFS is composed of successive eddies generated along the lower and upper walls as shown on Figure 9 for the pressure and vorticity fields obtained at times $t = 10$, 20 and 60. Only the two main eddies corresponding to the separation region just behind the step and the additional recirculating zone located on the upper wall remain after time $t = 60$. Far downstream the flow relaxes to the parabolic Poiseuille regime.

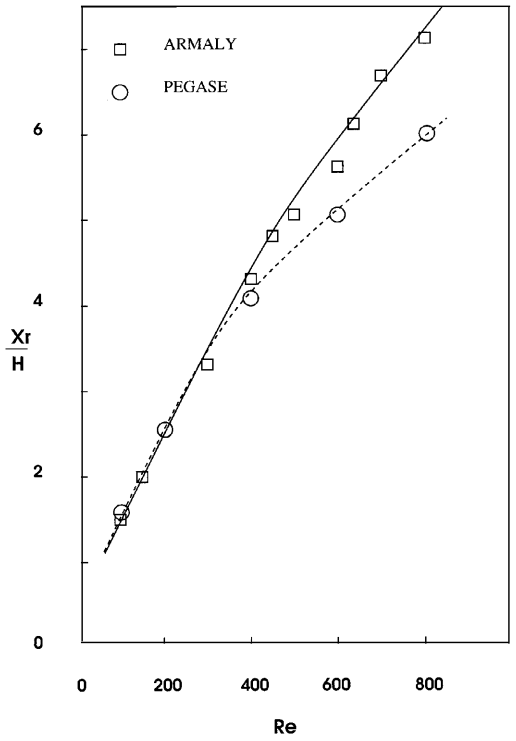

Figure 8. Reattachment length in laminar regime ($100 \leqslant Re \leqslant 800$)

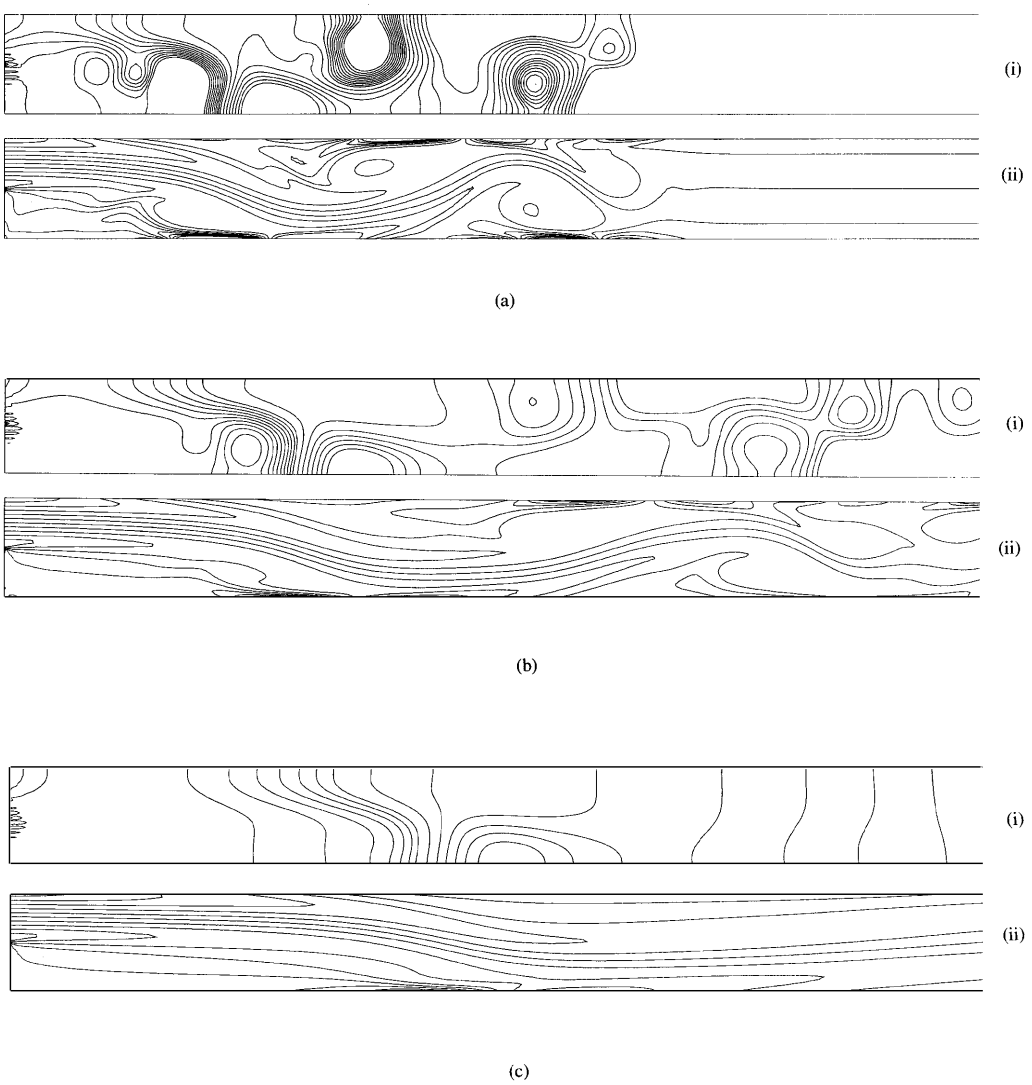

Figure 9. Transient flow fields. (a) $t = 10$; (i) pressure; (ii) vorticity. (b) $t = 20$: (i) pressure; (ii) vorticity. (c) $t = 60$: (i) pressure; (ii) vorticity

Time history plots of the streamwise and normal velocity components at six different positions in the flow field are shown in Figures 10 and 11. Two stations ($x/H = 6$ and 12) are given in the streamwise direction and three stations ($z/H = -0{\cdot}4, 0{\cdot}0$ and $0{\cdot}3$) in the normal directions.

The results show that, in agreement with the results of Gresho *et al.*, the flow evolves towards a steady state. This is confirmed by the kinetic energy time history plot in Figure 12, for which the relative change over the last 100 time units is less than 0·0001. Both transient and steady states are qualitatively in good agreement with the time history plots of the streamwise velocity component given by Gresho *et al.*[11] The same number and values of relative maxima are found, corresponding to the formation and collapse of near-wall eddies.

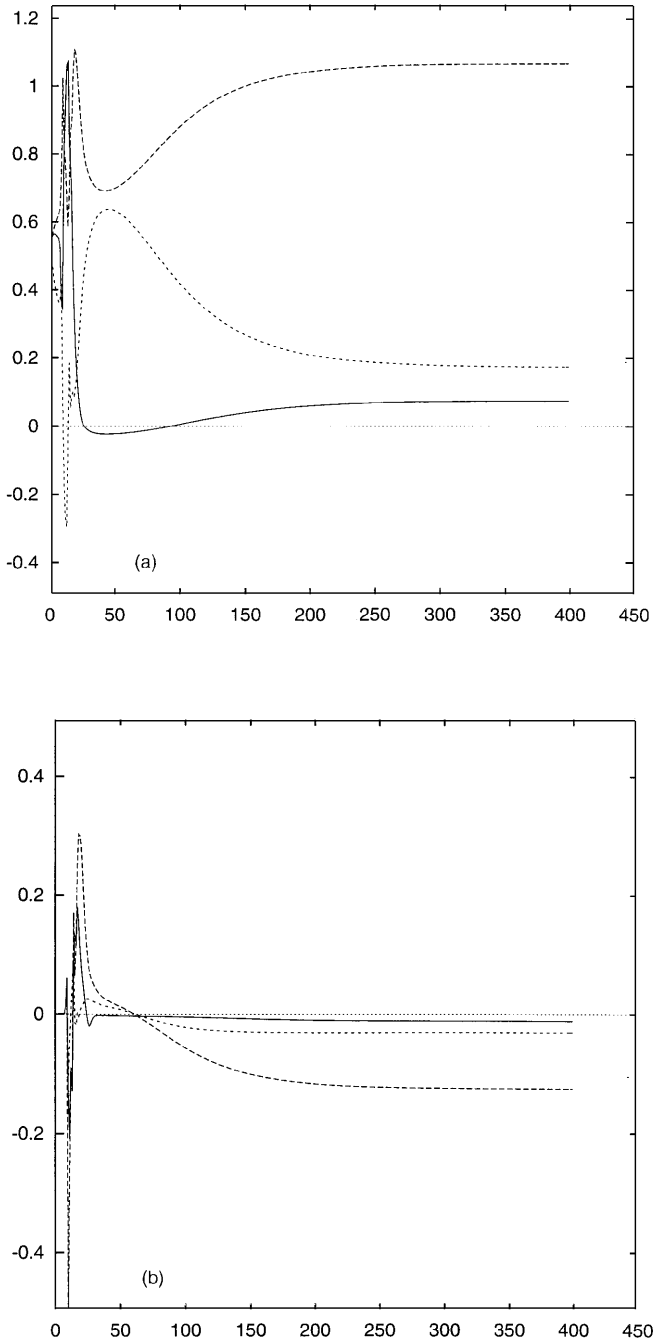

Figure 10. Velocity time history plots ($x/H = 6$). (a) u-component versus time: . . . ., $z/H = -0{\cdot}4$; - - - -, $z/H = 0$; ————, $z/H = 0{\cdot}3$. (b) w-component versus time: . . . .,$z/H = -0{\cdot}4$; - - - -, $z/H = 0$; ————, $z/H = 0{\cdot}3$

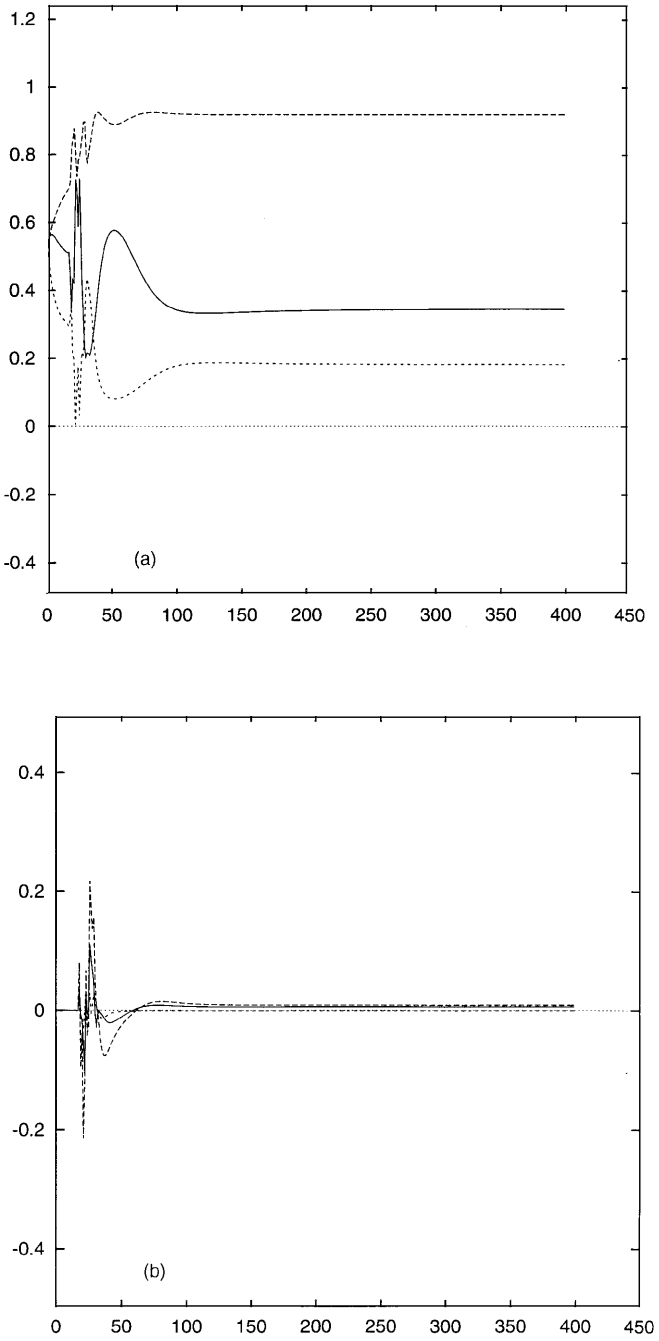

Figure 11. Velocity time history plots ($x/H = 12$). (a) u-component versus time: . . . ., $z/H = -0{\cdot}4$; - - - -, $z/H = 0$; ————, $z/H = 0{\cdot}3$. (b) w-component versus time: . . . .,$z/H = -0{\cdot}4$; - - - -, $z/H = 0$; ————, $z/H = 0{\cdot}3$

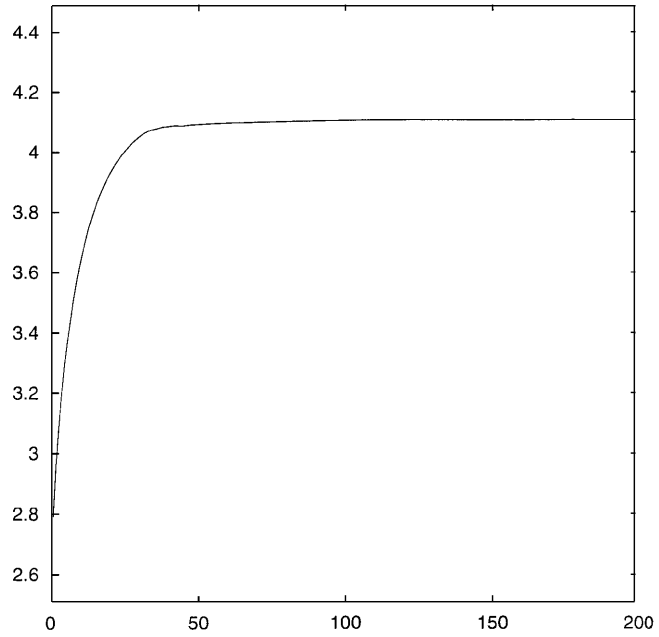

Figure 12. Total kinetic energy time history plot. Total kinetic energy versus time $t \leqslant 200$

6.3.3. Steady state regime. With the present time-dependent method the steady state is reached at about $t = 200$. The present results are illustrated in Figure 13 by pressure and vorticity distribution plots at time $t = 400$. Figure 14 displays the streamwise and normal velocity profiles across the channel at locations $x/H = 7$ and 15. As may be observed, the results are indistinguishable from those of Gartling obtained with a steady approach.[12] In fact, a very small difference exists for the w-component: the present results at $x/H = 6{\cdot}925$ coincide with Gartling's results at $x/H = 7$ (Figure 14(b)). Figure 15 shows the pressure and shear stress profiles along the lower and upper channel walls, which are also in good agreement with Gartling's results.

6.4. Influence of outflow boundary condition

The influence of the outflow boundary condition was studied by investigating, again at $Re = 800$, the effect of the truncation of the computational domain for two different values of the channel length L/H. The results of two computations corresponding to $L/H = 20$ and 7 are compared in Figure 16 at

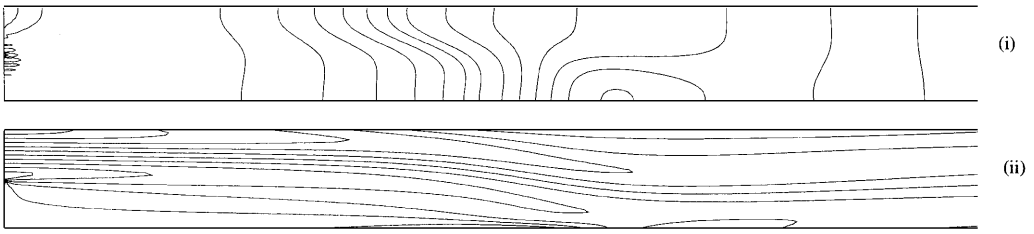

Figure 13. Steady state flow field at $t = 400$ ($L = 20$). (i) Pressure iso-contours. (ii) Vorticity iso-contours

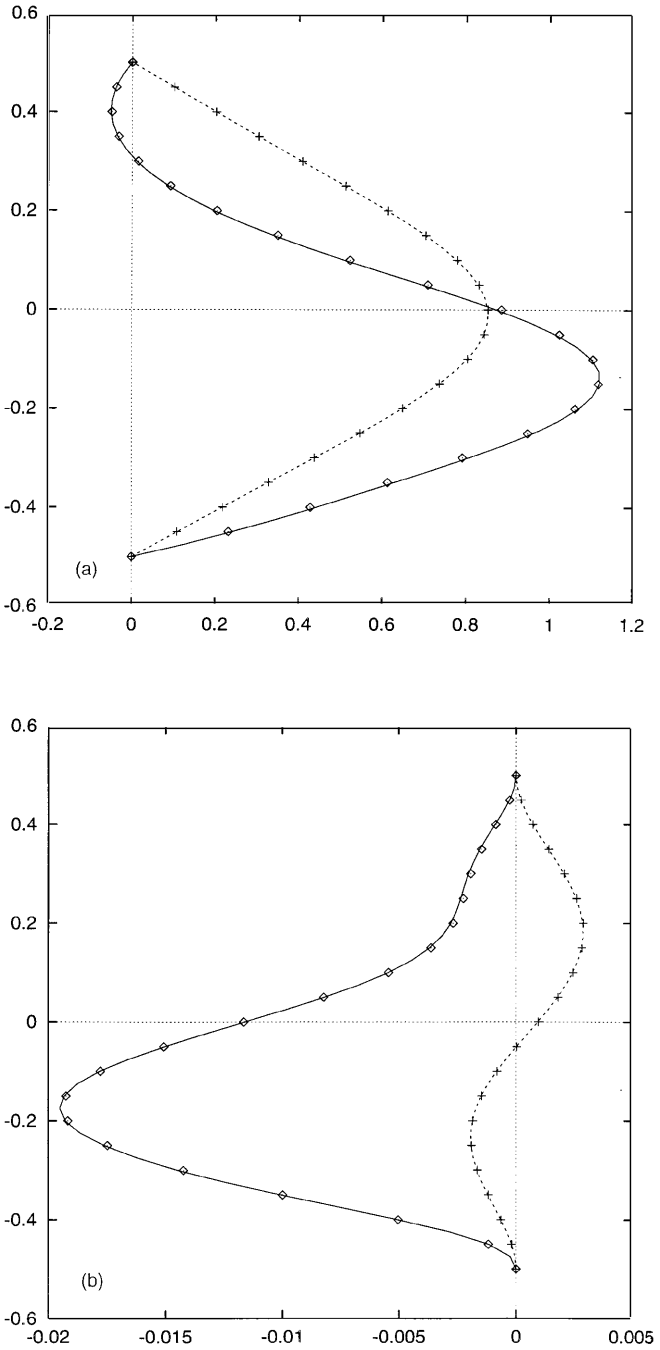

Figure 14. Steady state flow field at $t = 400$. (a) u-velocity component distribution (Z-co-ordinate versus u). Gartling: $\diamond$, $x/H = 7$; $+$, $x/H = 15$. Present method: ————, $x/H = 7$; - - - -, $x/H = 15$. (b) w-velocity component distribution (Z-co-ordiante versus w). Gartling: $\diamond$, $x/H = 7$, $+$, $x/H = 15$. Present method: ————, $x/H = 6{\cdot}925$; - - - -, $x/H = 15$

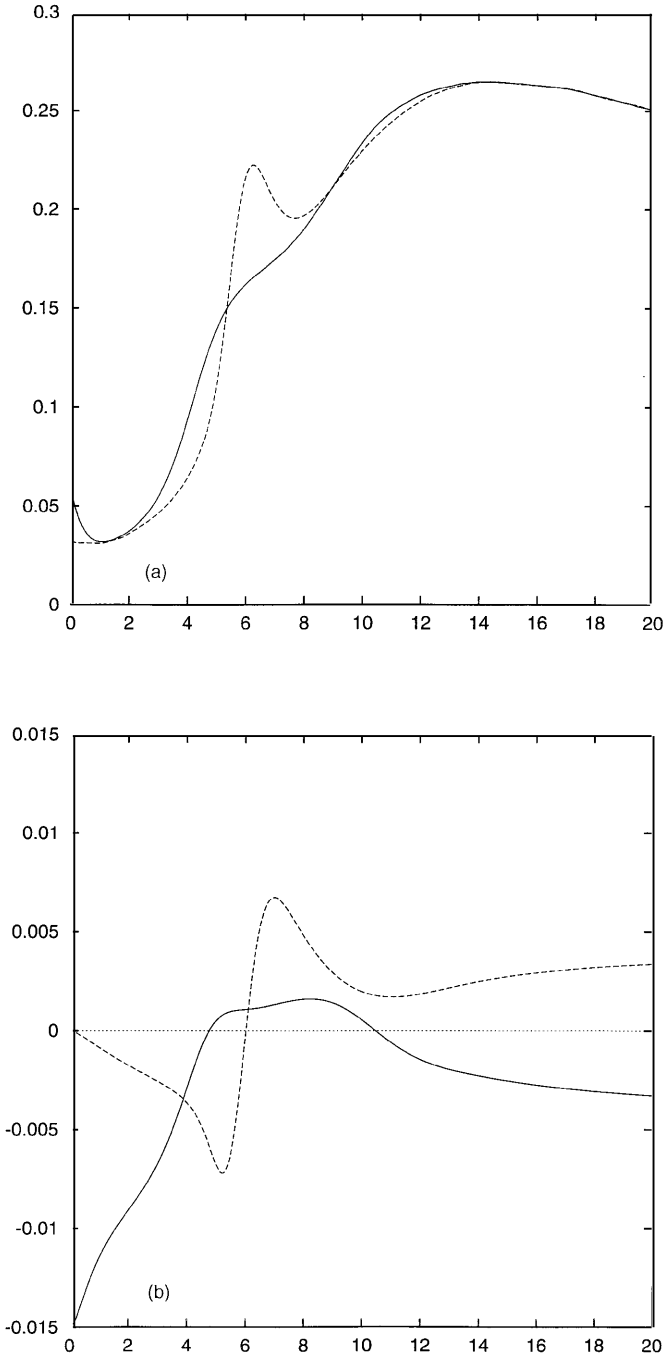

Figure 15. Steady state flow field at $t = 400$. Present method: ————, upper wall; - - - -, lower wall. (a) Wall pressure distribution (pressure versus X-co-ordinate). (b) Wall shear stress distribution (shear stress versus X-co-ordinate)

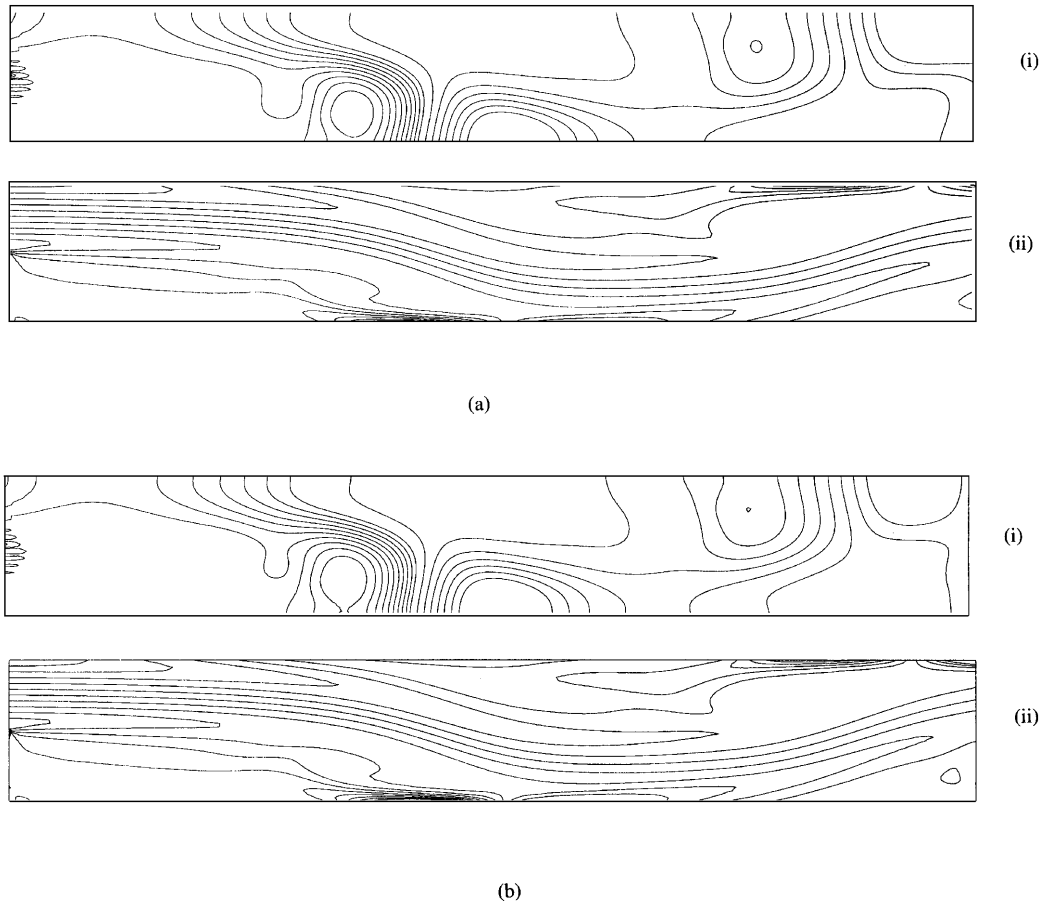

Figure 16. Influence of outflow boundary condition at $t = 20$. (a) Outflow boundary at $L = 20$: (i) pressure iso-contours; (ii) vorticity iso-contours. (b) Outflow boundary at $L = 7$: (i) pressure iso-contours; (ii) vorticity iso-contours

time $t = 20$. The two vorticity distributions are quasi-identical over a large part of the computational domain ($0 \leqslant x/H \leqslant 6$), while small pressure differences may be observed. The same conclusions may be reached at time $t = 400$ (Figure 17). The wall pressure and wall shear stress are also very influenced over $0 \leqslant x/H \leqslant 6$ by the outflow boundary condition (Figure 18).

Time history plots of the streamwise and normal velocity components at $x/H = 6$ are reported in Figure 19. In general, errors less than 10 per cent are encountered in these quantities at time $t = 400$ due to the outflow boundary condition. Nevertheless, the mean features of the separated flow as well as the steadiness of the solution have been preserved by the computation.

7. 3D RIBBED CHANNEL FLOW

The feasibility of the method for 3D computations is illustrated here by computating the flow at Reynolds number $Re = 50$ through a three-dimensional channel of square cross-section containing two ribs on the lower wall. Note that the low Reynolds number of the computation does not in any case alter the meaning of the demonstration: higher-Reynolds-number flows may be computed with more grid points on more powerful machines if the σ_u/Re_u stability criterion is fulfilled.

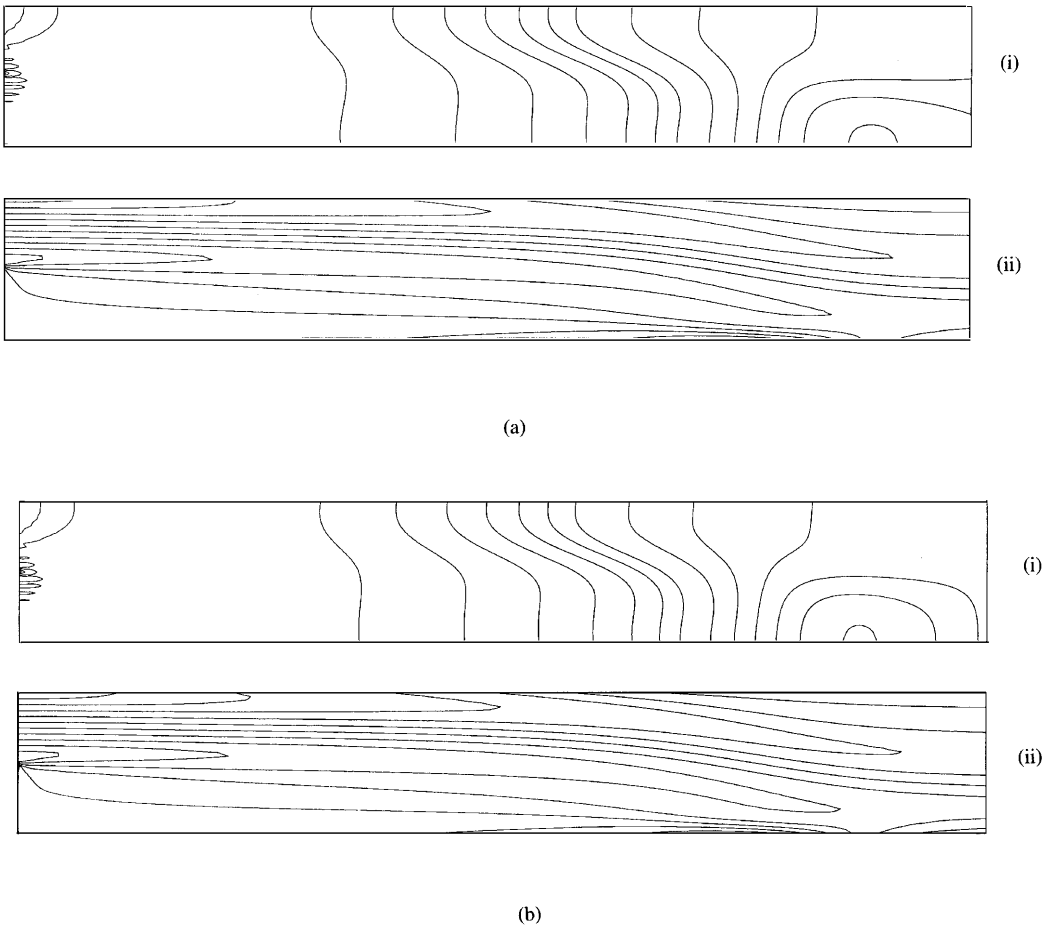

Figure 17. Influence of outflow boundary condition at $t = 400$. (a) Outflow boundary at $L = 20$: (i) pressure iso-contours; (ii) vorticity iso-contours. (b) Outflow boundary at $L = 7$: (i) pressure iso-contours; (ii) vorticity iso-contours

The computational domain, sketched in Figure 20, is defined as

$$\Omega = [a, b] \times [c, d] \times [e, f],$$

with

$$\partial\Omega = \Gamma_i \cup \Gamma_o \cup \Gamma_w.$$

Γ_i is the input boundary with an imposed Dirichlet boundary condition for the velocity (the velocity profile is given on this boundary), Γ_0 is the output boundary with a Neumann boundary condition for the velocity and Γ_w are the wall boundaries, where the no-slip condition is imposed.

7.1. Visualization of flow

The results presented here have been obtained at Reynolds number $Re = 50$ based on the maximal input velocity and the height of the ribs, with a Cartesian regular ($131 \times 41 \times 41$)-node mesh grid.

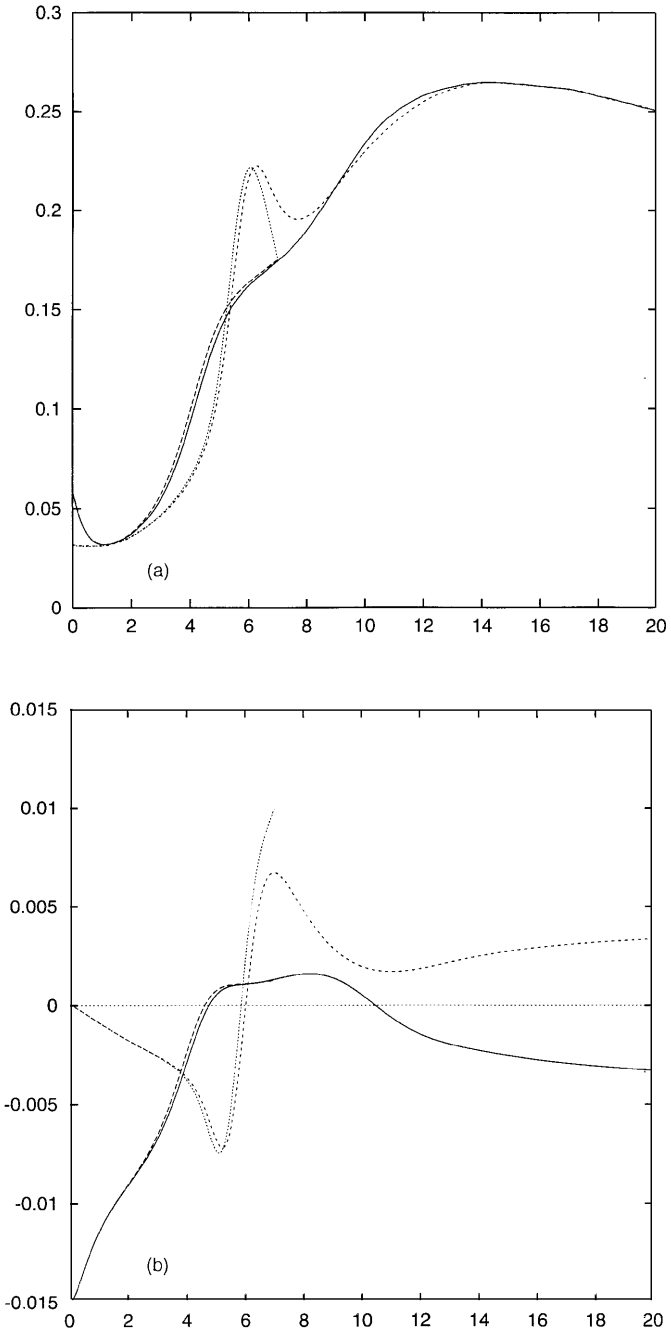

Figure 18. Influence of outflow boundary condition. Outflow boundary at $L = 20$: ————, lower wall; - - - -, upper wall. Outflow boundary at $L = 7$: - - - -, lower wall; . . . ., upper wall. (a) Wall pressure distribution (pressure versus X-co-ordinate). (b) Wall shear stress distribution (shear stress versus X-co-ordinate)

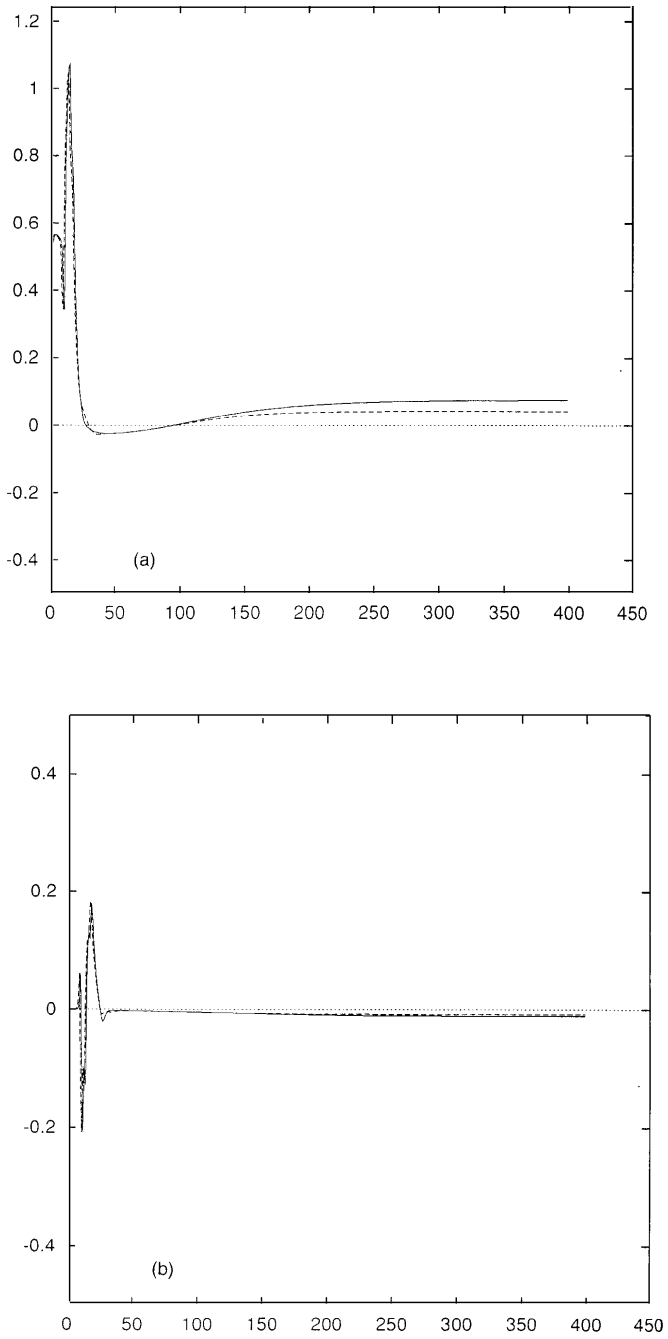

Figure 19. Influence of outflow boundary condition. Outflow boundary at $L = 20$: ————, $z/H = 0{\cdot}3$. Outflow boundary at $L = 7$: - - - -, $z/H = 0{\cdot}3$. (a) u-velocity component at $x/H = 6$ versus time ($t \leqslant 450$). (b) w-velocity component at $x/H = 6$ versus time ($t \leqslant 450$)

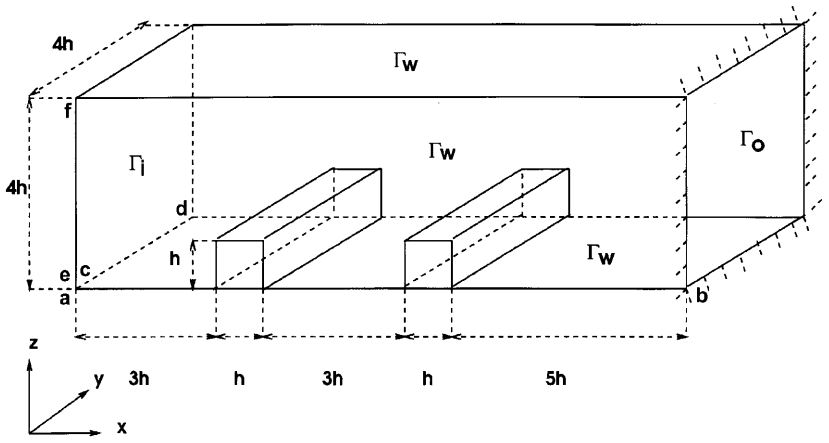

Figure 20. Ribbed square cross-section channel flow geometry and boundary conditions

Plate 1 shows a 3D view of the flow visualized by instantaneous streamlines at the non-dimensionalized time $t = 20$. The computation, performed with a time step $\Delta t = 10^{-2}$, required about 1·5 h on a CRAY YMP. One can see the highly three-dimensional character of the flow in the near-wall region between the ribs. Because of the lateral walls, the streamlines near the lower wall and lateral walls deviate towards the centre of the channel into the recirculating zone before going over the second rib.

Plate 2 shows two other points of view of the same flow.

7.2. Pressure distribution

Plate 3 displays the iso-pressure distributions in the symmetry plane $y = (c + d)/2$ of the channel as well as in the median plane $z = (e + f)/2$ at time $t = 20$. The computation has been carried out in a way satisfying the stability criteria obtained in Section 5.3. Hence the pressure field displays no spurious oscillations.

8. CONCLUSIONS

A new spatial scheme based on Q1 isoparametric finite elements has been proposed to discretize the divergence operators involved in the projection method used to solve the Navier–Stokes equations for incompressible fluids.

This scheme, which forms the kernel of the PEGASE Navier–Stokes solver developed at ONERA for the discrete simulation of viscous flows, has interesting smoothing and stability properties. Associated with finite-difference-type treatments of boundary conditions, it has been used with success for stimulating 2D and 3D separated flows.

Detailed validation tests conducted for the backward-facing step problem have shown the efficiency of the present method for long-term unsteady computations.

Current studies are aimed at applying the present hybrid finite element methodology to curvilinear body-fitted mesh grids.

ACKNOWLEDGEMENTS

The authors thank M. O. Deville for useful discussions. Partial support by DRET (Direction des Recherches et Etudes et Techniques) is gratefully acknowledged.

APPENDIX: STABILITY STUDY

Fourier analysis of the scheme provides conditions for no error growth (when all error modes are damped), which are conditions for practical stability in the unsteady problem. Forgetting as usual the boundary conditions and the specific instabilities arising from the non-linear convection term, we consider the linear two-dimensional scalar advection–diffusion problem

$$\frac{\partial \Phi}{\partial t} + \vec{V} \cdot \vec{\nabla} \Phi = \nu \nabla^2 \Phi, \tag{48}$$

where the components (u, w) of $\vec{V}$ and ν are assumed to be non-negative.

Using a uniform mesh spacing Δx and Δz and a time step Δt, we discretize the advection terms with the hybrid scheme (19) and the Laplacian operator with the second-order centred scheme (22). Performing the time integration with the explicit forward Euler scheme, we obtain the following discrete form of equation at location $(i\Delta x, k\Delta z)$ for time $t = (n+1)\Delta t$:

$$\begin{aligned}\Phi_{i,k}^{n+1} = \Phi_{i,k}^n + \Delta t\Big(&-\frac{u}{12\Delta x}[4(\Phi_{i+1,k}^n - \Phi_{i-1,k}^n) + (\Phi_{i+1,k+1}^n - \Phi_{i-1,k+1}^n) + (\Phi_{i+1,k-1}^n - \Phi_{i-1,k-1}^n)] \\ &- \frac{w}{12\Delta z}[4(\Phi_{i,k+1}^n - \Phi_{i,k-1}^n) + (\Phi_{i+1,k+1}^n - \Phi_{i+1,k-1}^n) + (\Phi_{i-1,k+1}^n - \Phi_{i-1,k-1}^n)] \\ &+ \frac{\nu}{\Delta x^2}(-2\Phi_{i,k}^n + \Phi_{i+1,k}^n + \Phi_{i-1,k}) + \frac{\nu}{\Delta z^2}(-2\Phi_{i,k}^n + \Phi_{i,k+1}^n + \Phi_{i,k-1}^n)).\end{aligned} \tag{49}$$

Using modal decomposition,

$$\Phi_{i,k}^n = A_{i,k}^n \mathrm{e}^{\mathrm{j}i2\pi/N} \mathrm{e}^{\mathrm{j}k2\pi/N}, \quad 0 \leqslant i, k \leqslant N, \quad j = \sqrt{(-1)},$$

where $A_{i,k}^n$ is the amplitude of the harmonic (i, k) at time step n. Equation (49) leads to the following relation for the amplitude $A_{i,k}^{n+1}$:

$$\begin{aligned}A_{i,k}^{n+1} = A_{i,k}^n \Bigg[&\left(1 - 2\frac{\nu\Delta t}{\Delta x^2}(1 - \cos\phi_i) - 2\frac{\nu\Delta t}{\Delta z^2}(1 - \cos\phi_k)\right) \\ &- \mathrm{j}\left(\frac{\Delta t}{3\Delta x} u \sin\phi_i(2 + \cos\phi_k) + \frac{\Delta t}{3\Delta z} w \sin\phi_k(2 + \cos\phi_i)\right)\Bigg],\end{aligned} \tag{50}$$

where the phase angles ϕ_i and ϕ_k are respectively equal to $i2\pi/N$ and $k2\pi/N$ and belong to the range $[0, 2\pi]$.

The corresponding amplification factor $G(i, k)$, defined as

$$G(i, k) = \frac{A_{i,k}^{n+1}}{A_{i,k}^n},$$

is in this case

$$\begin{aligned}G(i, k) = 1 &- 2\frac{\sigma_u}{Re_u}(1 - \cos\phi_i) - 2\frac{\sigma_w}{Re_w}(1 - \cos\phi_k) \\ &- \mathrm{j}\left(\frac{\sigma_u}{3}\sin\phi_i(2 + \cos\phi_k) + \frac{\sigma_w}{3}\sin\phi_k(2 + \cos\phi_i)\right),\end{aligned} \tag{51}$$

where

$$Re_u = \frac{u\Delta x}{\nu}, \qquad Re_w = \frac{w\Delta z}{\nu} \tag{52}$$

are respectively the u- and w-based cell Reynolds numbers and

$$\sigma_u = \frac{u\Delta t}{\Delta x}, \qquad \sigma_w = \frac{w\Delta t}{\Delta z} \tag{53}$$

are the CFL numbers based on the two components of the convecting velocity.

From (51) we write

$$|G|^2 = \left(1 - 2\frac{\sigma_u}{Re_u}(1-\cos\phi_i) - 2\frac{\sigma_w}{Re_w}(1-\cos\phi_k)\right)^2 + \left(\frac{\sigma_u}{3}\sin\phi_i(2+\cos\phi_k) + \frac{\sigma_w}{3}\sin\phi_k(2+\cos\phi_i)\right)^2. \tag{54}$$

Using the equality

$$\tfrac{1}{3}(2+\cos\phi_i) = \tfrac{1}{3}[3-(1-\cos\phi_k)] = 1 - \tfrac{2}{3}\sin^2(\phi_k/2)$$

leads to

$$|G|^2 = \left(1 - 2\frac{\sigma_u}{Re_u}(2-\cos\phi_i) - 2\frac{\sigma_w}{Re_w}(2-\cos\phi_k)\right)^2 + \left[\sigma_u\sin\phi_i\left(1-\frac{2}{3}\sin^2\frac{\phi_k}{2}\right) + \sigma_w\sin\phi_k\left(1-\frac{2}{3}\sin^2\frac{\phi_i}{2}\right)\right]^2. \tag{55}$$

Note that we have $\forall\phi_i, \forall\phi_k$

$$\sigma_u\left(1-\frac{2}{3}\sin^2\frac{\phi_k}{2}\right) \leqslant \sigma_u, \qquad \sigma_w\left(1-\frac{2}{3}\sin^2\frac{\phi_i}{2}\right) \leqslant \sigma_w$$

and the theorem established by Hindmarsh *et al.*[21] can be used, leading to the criterion

$$\Delta t \leqslant \mathrm{Min}(\alpha;\beta), \tag{56}$$

with

$$\alpha = \frac{2\nu}{u^2+w^2}, \qquad \beta = \frac{1}{2\nu(1/\Delta x^2 + 1/\Delta z^2).} \tag{57}$$

REFERENCES

1. J. A. Chorin, 'A numerical method for solving incompressible viscous flow problems', *J. Comput. Phys.*, **2**, 12–26 (1967).
2. F. H. Harlow and J. E. Welch, 'Numerical calculation of time-dependent viscous incompressible flow of fluid with free surface', *Phys. Fluids*, **8**, 2181–2189 (1965).
3. J. A. Chorin, 'Numerical solution of the Navier–Stokes equations', *Math. Comput.*, **22**, 745–762 (1968).
4. J. C. Strikwerda, 'Finite difference methods for the Stokes and Navier–Stokes equations', *SIAM J. Sci. Stat. Comput.*, **5**, 56–68 (1984).
5. S. W. Armfield, 'Finite difference solution of the Navier–Stokes equations on staggered and non-staggered grids', *Comput. Fluids*, **20**, 1–17 (1991).
6. F. Sotiropoulos and S. Abdallah, 'The discrete continuity equation in primitive variable solutions of incompressible flow', *J. Comput. Phys.*, **95**, 212–227 (1991).
7. C. M. Rhies and W. L. Chow, 'Numerical study of the turbulent flow past an airfoil with trailing edge separation', *AIAA J.*, **21**, 1525–1532 (1983).

8. S. Abdallah, 'Numerical solutions for the pressure Poisson equation with Neumann boundary conditions using a non-staggered grid, I', *J. Comput. Phys.*, **70**, 182–192 (1987).
9. S. Abdallah, 'Numerical solutions for the pressure Poisson equation with Neumann boundary conditions using a non-staggered grid, II', *J. Comput. Phys.*, **70**, 193–202 (1987).
10. P. M. Gresho and R. L. Sani, 'On pressure boundary conditions for the incompressible Navier–Stokes equations', *Int. j. numer methods fluids*, **7**, 1111–1145 (1987).
11. P. M. Gresho, D. K. Gartling, J. R. Torczynski, K. A. Cliffe, K. H. Winters, T. J. Garratt, A. Spence and J. W. Goodrich, 'Is the steady viscous incompressible two-dimensional flow over a backward-facing step at $Re = 800$ stable?', *Int. j. numer. methods fluids*, **17**, 501–541 (1993).
12. D. K. Gartling, 'A test problem for outflow boundary conditions—flow over a backward-facing step', *Int. j. numer. methods fluids*, **11**, 953–967 (1990).
13. P. M. Gresho, 'Incompressible fluid dynamics: some fundamental formulation issues', *Ann. Rev. Fluid. Mech.*, **23**, 413–453 (1991).
14. P. M. Gresho, 'Some current CFD issues relevant to the incompressible Navier–Stokes equations', *Comput. Methods Appl. Mech. Eng.*, **87**, 201–252 (1991).
15. C. Hirsch, *Numerical computation of Internal and External Flows*, Wiley, Chichester, 1988.
16. C. A. J. Fletcher, *Computational Technique for Fluid Dynamics*, Springer, New York, 1988, pp. 355–360.
17. B. Gustafsson, 'The convergence rate for difference approximations to mixed initial boundary value problem', *Math. Comput.*, **29**, 396–406 (1975).
18. S. A. Orszag, M. Israeli and M. Deville, 'Boundary conditions for incompressible flows' *J. Sci. Comput.*, **1**, 75–111 (1986).
19. J. L. Guermond, 'Some error estimates for the approximation of the unsteady Navier–Stokes equations by means of projection methods', *SIAM J. Numer. Anal.*, submitted.
20. H. Van der Vorst, 'Bi-CGSTAB: a fast and smoothly converging variant of Bi-CG for the solution of nonsymmetric linear systems', *SIAM J. Sci. Stat. Comput.*, **13**, 631–644 (1992).
21. A. C. Hindmarsh, P. M. Gresho and D. F. Griffiths, 'The stability of explicit Euler time-integration for certain finite difference approximations of the multidimensional advection–diffusion equation', *Int. j. numer. methods fluids*, **4**, 853–897 (1984).
22. R. L. Sani and P. M. Gresho, 'Résumé and remarks on the open boundary condition minisymposium', *Int. j. numer. methods fluids*, **18**, 983–1008 (1994).
23. B. F. Armaly, F. Durst, J. C. Pereira and B. Schonung, 'Experimental and theoretical investigation of backward-facing step', *J. Fluid Mech.*, **127**, 473–496 (1983).

